RESEARCH ARTICLE

Dendrite-free lithium electrodeposition enabled by 3D porous lithiophilic host toward stable lithium metal anodes

Linghong Xu, Zhihao Yu and Junrong Zheng ⓘ *

College of Chemistry and Molecular Engineering, Peking University, 100871, Beijing, P R China.

*Correspondence address. College of Chemistry and Molecular Engineering, Peking University, 100871, Beijing, PR China. Tel: 010 62753815; E-mail: junrong@pku.edu.cn

Abstract

Lithium metal is a promising anode utilized in cutting-edge high-energy batteries owing to the low density, low electrochemical potential, and super high theoretical capacity. Unfortunately, continuous uncontrollable lithium dendrite growth and 'dead' lithium result in capacity decay, low coulombic efficiency and short circuit, severely hindering the practical utilization of lithium anode. Herein, we propose a three-dimensional porous lithiophilic current collector for lithium storage. The conductive 3D structure constructed by carbon fiber (CF) can well accommodate the deposited lithium, eliminating volume change between the lithium depositing/stripping process. Moreover, the polydopamine (PDA) coating on the CF surface possesses a large number of polar groups, which can homogenize Li^+ ions distribution and apply as the sites for lithium deposition, decreasing nucleation overpotential. As a result, under the 1 mA cm^{-2} current density, the PDA coated CF (PDA@CF) electrode exhibits high CE (~98%) for 1000 cycles. Galvanostatic measurements demonstrate that the Li anode using PDA@CF achieves 1000 h cycling life under 1 mA cm^{-2} with a low overpotential (<15 mV). The LiFePO$_4$ full cell shows enhanced rate performance and stable long-term cycling.

Key words: lithium metal; lithium metal battery; lithium dendrites; 3D host; polydopamine; carbon fiber.

INTRODUCTION

Rechargeable lithium-ion batteries have been extensively utilized in various fields, including small electronic equipment, electric vehicles and energy storage grid [1]. However, due to the relatively low specific capacity of traditional electrodes, such as graphite electrodes (372 mAh g^{-1}), it is difficult to satisfy the expanding demand for more capacity and power [2]. To address this difficulty, lithium metal battery (LMB) are considered as an ideal substitute owing to their high energy density. Compared to other anode materials, lithium metal has an unprecedented theoretical capacity of 3860 mAh g^{-1} and the lowest electrochemical potential

(−3.04 V vs. the SHE) [3]. Therefore, lithium metal is relied upon to supplant graphite as the first choice of the next generation high-energy Li-S and Li-O$_2$ batteries [4, 5].

As early as 1976, lithium anode has already been studied and fabricated by Exxon [6]. Unfortunately, its cycling instability and safety concerns limit the commercialization of lithium metal batteries. Unlike lithium intercalation compounds, lithium ions are directly deposited on the lithium anode surface during charging, so the surface morphology has a great impact on the lithium-ion deposition behaviors [7]. There may be an uneven local Li^+ flux between the electrolyte and electrode because of the rugged

morphology. Subsequently, Li^+ tends to plate on the protrusions of the electrode, leading to the formation of lithium dendrite, further increasing the surface roughness [8, 9]. Besides, the solid electrolyte interface (SEI) can not accommodate the tremendous volume change of lithium metal in the cycling process, which falls into repeated rupture and regeneration, prompting capacity loss, low coulombic efficiency (CE) and lifetime degradation [10, 11]. The uncontrollable sharp dendrites can poke through the separator, eventually causing the short circuit [12].

Different electrolyte additives have been created to optimize the liquid electrolytes, including fluoroethylene carbonate [13–15], Cs^+ ions [16, 17], CO_2 [18], LiF [19, 20] and ionic liquid [21, 22]. These additives participate in the formation of SEI, improving its uniformity and stability. However, in most cases, the additives are continuously consumed during cell cycling, which is difficult to remain sustainable over a long period of time [23, 24]. Artificial protective SEI films coated on the out layer of lithium ex situ are also developed. The protective layer is usually composed of polymers or inorganic materials, such as Cu_3N+SBR layer [25], LiF/PVDF-HFP composite film [26] and lithium silicate (Li_xSiO_y) [27], which has good chemical stability and mechanical properties to restrain the formation of lithium dendrite. However, owing to the high reactivity of lithium metal, the coating process may be cost unfriendly, which is not suitable for mass production. The solid electrolyte, considered an ideal choice for lithium metal anode, has reliable mechanical strength and can inhibit the growth of lithium dendrites in a physical barrier way [28, 29]. Nevertheless, the solid electrolyte often leads to higher polarization voltages owing to their high interfacial impedance and low ionic conductivity [30, 31].

In addition to the above strategies, the modifications on the current collector have also been extensively studied to defeat the drawbacks of lithium anode [32, 33]. These modifications are mainly to construct current collector with a 3D structure, which could increase the electrode surface area and reduce the local current density [34, 35]. Simultaneously, empty space inside the 3D structure can well accommodate the deposited lithium, greatly eliminating the negative impact of volume change [36]. Herein, we propose a novel electrode with 3D porous lithiophilic host to stabilize lithium metal. The modified current collector not only has the advantages of the 3D structure but also introduces polydopamine (PDA) to improve the lithophilicity of the current collector. The host structure is mainly composed of carbon fiber (CF) coated with strong adhesive PDA. The PDA coating layer, possessing lithiophilic functional groups (such as hydroxyl and amino), is expected to serve as lithium nucleation sites, thereby realizing uniform lithium distribution and deposition. Under the synergy of the 3D CF and PDA, the modified current collector effectively improves the deposition behaviors of Li^+ and suppresses the growth of lithium dendrites. The prelithified PDA coated CF (PDA@CF) electrode shows outstanding cycle life, high CE and low overpotential. When paired with $LiFePO_4$, the full cells exhibit excellent capacity retention and superior cycle stability.

EXPERIMENTAL SECTION

Preparation of lithium polyacrylate

Lithium polyacrylate (LiPAA) was prepared by ion exchange reaction. A 10% polyacrylic acid (PAA) solution was prepared by dissolving PAA (average Mv $\sim$250 000, Sigma-Aldrich) in deionized water. Then the aqueous solution of lithium

hydroxide (98%, Aladdin) of equal molar amount was added to PAA drop by drop for a final solution pH $\approx$ 7. Then, the prepared LiPPA solution was placed in an open container to allow the majority of water to evaporate, followed by vacuum drying under 60°C for 24 h.

PDA@CF preparation

The CFs (purchased from MREDA) were dispersed in the dopamine (98%, Aladdin) solution (10 mM in methanol) with the Tris-HCl buffer (10 mM, pH 8.5). After stirring at 800 rpm for 2 h and standing at room temperature for 24 h, the products were filtrated, followed by ethanol washing, and vacuum dried under 50°C for 24 h, which was denoted as PDA@CF. The PDA layer is about 80 nm thick.

Material characterization

The field emission scanning electron microscope (Hitachi S-4800) was utilized to obtain scanning electron micrographs (SEMs). The JEM-2100F microscope was used to obtain high-resolution TEM (HRTEM) images and EDS images. An AXIS Supra (Kratos Analytical Ltd., UK) was applied to obtain X-ray photoelectron spectrometer (XPS) element analysis while using Al Kα X-ray as radiation source. The Rigaku Ultima was utilized to collect the X-ray diffraction (XRD) pattern. The FTIR spectrophotometer (Thermo Fisher Scientific) was used to characterize the chemical structure of the PDA. The DXRxi (Thermo Fisher Scientific) was applied to collect the Raman spectra. To observe Li deposition morphology, Li/Cu cells were disassembled after different electrochemical processes (dissolution/deposition). Then the lithium foil to be tested was gently washed with 1,2-dimethoxyethane 3 times to eliminate the residual electrolyte, and then followed by vacuum drying.

Electrochemical measurements

To prepare the electrodes, the PDA@CF and LiPAA were stirred in distilled water with the mass ratio of 2:1 for 12 h to get a homogenous slurry. Then, the slurry was cast onto a copper foil by a doctor blade. After vacuum drying under 60°C for 24 h, the PDA@CF electrode was obtained.

Coin-type cells (CR-2032) were utilized in this work, while the working electrode is PDA@CF electrode or Cu and the counter electrode is the Li metal foil. The electrolyte is 1 M lithium bis(trifluoromethanesulfonyl)imide in DOL/DME (1:1 v/v) with 2 wt% $LiNO_3$. Electrochemical analyzer (CHI650C) was utilized for the impedance measurements and LANHE CT2001A battery tester was used in the cycling measurements.

To evaluate the cycling performance, Li of 6 mAh cm^{-2} was pre-deposited into the pristine Cu and PDA@CF electrodes using the half cell, obtaining the Cu-Li and PDA@CF-Li electrodes, respectively. Then the Cu-Li and PDA@CF-Li electrodes were extracted from the half cells and assembled into the symmetrical cell, respectively. Galvanostatic cycling was conducted at various current densities, and the voltage was recorded with time. Electrochemical impedance spectra (EIS) were measured with an amplitude voltage of 5 mV at room temperature, and the frequency range was set in 0.1 Hz $\sim$ 1 MHz.

To test the full cell, $LiFePO_4$ (LFP) was utilized as cathode material. LFP, polyvinylidene difluoride, acetylene black (weight ratio of 85:10:5) were mixed in the solvent of N-methylpyrrolidone (NMP). After being stirred for 24 h, the homogenous slurry was cast on aluminum collector by a doctor blade. After vacuum
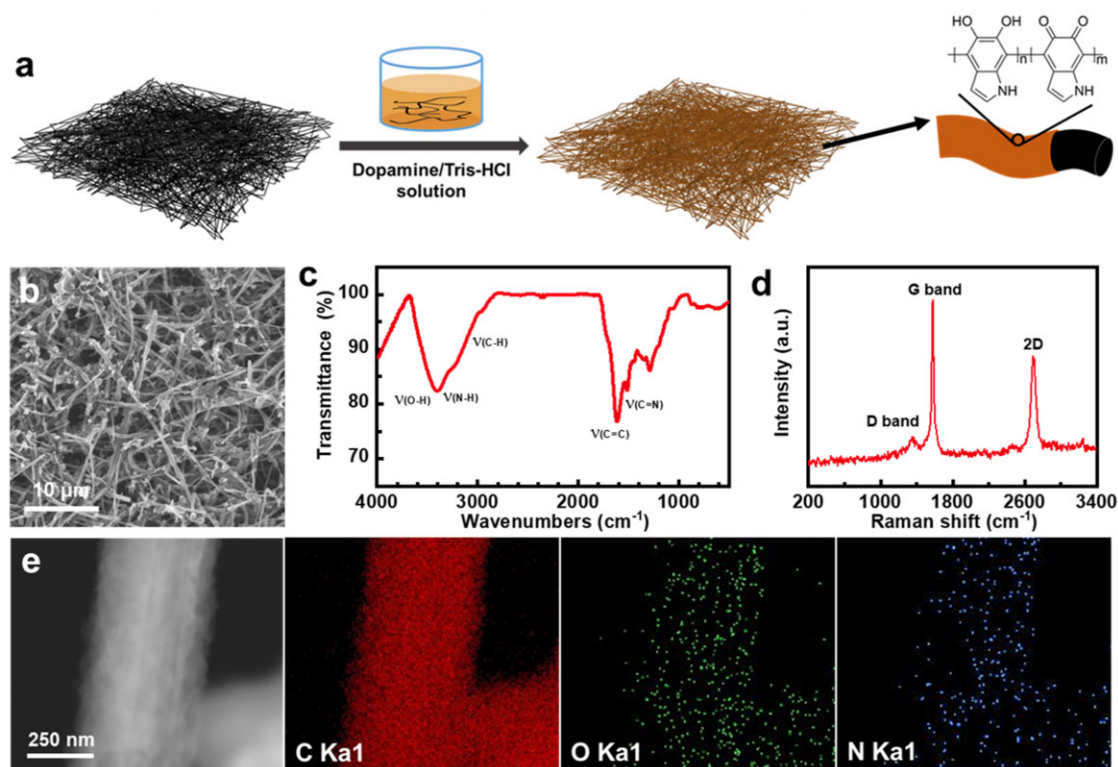
Figure 1: (a) Fabrication process of the PDA@CF. (b) SEM image, (c) FTIR spectrum, (d) Raman spectrum, (e) HRTEM image and elemental mapping for the C, O, N of the PDA@CF.

drying under 100°C for 24 h, the LFP cathode was obtained (mass loading ~6 mg cm^{-2}).

RESULT AND DISCUSSION

Figure 1a schematically illustrates the fabrication procedure of the PDA@CF. The CFs were immersed in the dopamine-tris(hydroxymethyl)aminomethane-HCl buffer solution to allow dopamine (DA) to self-polymerize and deposit on the surface of CF. Subsequently, the PDA@CF electrodes were prepared with the typical slurry-making process using polymer lithium polyacrylate (LiPAA) as binder. The PDA@CF has a cross-linked 3D porous structure, shown in the SEM image (Fig. 1b). FTIR spectrum of the prepared PDA is shown in Fig. 1c. The broad absorption peaks at 3700–3300 cm^{-1} are ascribed to ν(N-H) and ν(O-H) stretching modes, the aliphatic ν(C-H) stretching modes are at around 2900 cm^{-1}. The absorption peaks around 1614 and 1518 cm^{-1} are attributed to the ν_{ring}(C=C) of indoline structure and ν_{ring}(C=N) stretching vibration of indole structure in the PDA. Raman spectrum (Fig. 1d) shows three characteristic bands of carbon, which are the 2D band at 2698 cm^{-1}, the G band at 1580 cm^{-1} and the D band at 1355 cm^{-1}. The presence of 2D band indicates that the carbon material has a graphene-like structure. Besides, the intensity ratio of D band to G band ($I_D/I_G =$ 0.122) indicates insignificant defects in the carbon material, which is coincided with a sharp peak (002) in the XRD pattern (Supplementary Fig. S1). XPS was employed to detect the elements change of the CF after PDA modification (Supplementary Fig. S2). The existence of O and N peaks in PDA@CF indicates that PDA coating has been successfully introduced to the surface of CFs. Besides, the HRTEM and elemental mapping results

of the modified CFs further confirm the uniform element distribution in PDA@CF (Fig. 1e).

The Li plating morphology is a significant factor to assess the Li electrochemical behaviors on the electrode. Galvanostatic cycling of the Li/PDA@CF half cell was carried under a current density of 0.5 mA cm^{-2} and the voltage was recorded with time (Fig. 2a). During the process of lithium deposition, the insertion process of Li$^+$ into CFs is reflected in the voltage drop from $\sim$ 1 V to -0.025 V. The capacity contributed by the intercalation does not exceed 0.5 mAh cm^{-2}. Subsequently, the voltage plateau at -0.02 V is ascribed to the stable nucleation and deposition stage of Li$^+$ on the surface of CF. The morphological evolution of lithium deposition within PDA@CF was analyzed by SEM. The surface SEM images show that lithium was continuously deposited on the PDA@CF host and partially filled the porous structures (Fig. 2c). It can be observed that pancake-like Li deposited evenly on the electrode with the increase of Li deposition areal capacity (Fig. 2d and e). Especially at the edge of deposition, the lithium, embedded with fibers, shows a flat and smooth surface without any visible dendrites, indicating the good compatibility between lithium and PDA@CF (Supplementary Fig. S3c and d). The dendrite-free and compact lithium deposition is mainly ascribed to a 3D porous structure constructed by CFs and multiple deposition sites provided by PDA. On the one hand, the uniform distribution of Li$^+$ guided by lithiophilic sites in PDA ensures that the edges of deposited lithium have the same chance to contact with lithium ions, thus avoiding local over-deposition. On the other hand, the three-dimensional space formed by the CFs can well accommodate lithium. The synergy of the two factors positively affects the lithium deposition behaviors and prevents the formation of lithium dendrite. Besides, the deposited Li could be reversibly stripped from the PDA@CF as well. As
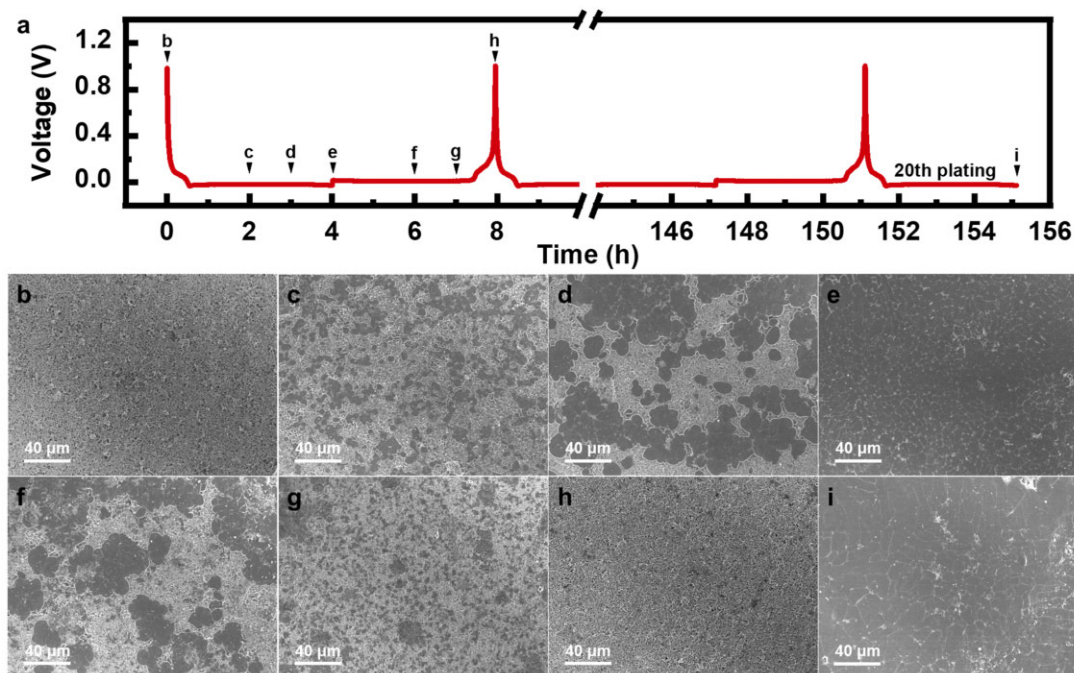
Figure 2: (a) The plating/stripping curves of PDA@CF electrode in the half cell at the 0.5 mA cm^{-2} current density. The surface SEM images of (b) original PDA@CF electrode and after depositing Li metal of (c) 2, (d) 3 and (e) 4 mAh cm^{-2}. The surface SEM images of PDA@CF electrode after stripping Li metal of (f) 2, (g) 3 and (h) 4 mAh cm^{-2} (that is, recharged to 1 V). (i) The surface SEM image of PDA@CF electrode (with the deposited lithium of 4 mAh cm^{-2}) after 20 cycles.

shown in Fig. 2f–h, along with the charging process, the Li was continuously stripped from the PDA@CF, and the pancake-like lithium became smaller. While the delithiation process was completed after charging to 1 V (Fig. 2h), the pancake-like lithium disappeared totally with the PDA@CF structure recovered to the initial state. The 3D structure of the CFs remains intact during the total cycling process, indicating the excellent robustness of PDA@CF, which is beneficial to long-term cycling. After continuous plating/stripping Li of 4 mAh cm^{-2} 20 times, the deposited lithium in PDA@CF electrode remains a flat surface without any observable Li dendrites, suggesting the outstanding electrochemical behaviors of Li. In contrast, the pristine Cu foil exhibited obvious lithium dendrites at the first deposition (Supplementary Fig. S4c). What is more, due to the low reversibility, a lot of lithium debris remained on the surface of the copper electrode after the stripping of lithium metal (Supplementary Fig. S4h). The residual debris further increased the non-uniformity of charge distribution on the electrode, resulting in the deterioration of the subsequent lithium deposition. After 20 cycles (Supplementary Fig. S4i), there were not only lithium dendrites, but also a significant amount of 'dead' lithium on Cu foil, which reflects the superiority of the 3D CFs structure and multiple deposition sites of PDA.

The Li nucleation overpotential (μ_n), defined as the voltage gap between the voltage dip and the subsequent plateau on the discharge profile, is introduced to quantitatively evaluate the lithiophilicity of electrodes. As shown in the discharge curves of the electrodes (Fig. 3a), the μ_n is only 15 mV for PDA@CF electrode at the 0.5 mA cm^{-2} current density while is that of 90 mV for copper foil. As the current density increase, the μ_n of copper foil increases drastically, which is 92 mV, 126 mV, and 136 mV at the current density of 1, 2 and 5 mA cm^{-2}, respectively, whereas the PDA@CF electrode always exhibits a relatively small μ_n below 25 mV, indicating the lower energy barrier for Li nucleation in electrochemically plating. This could be attributed

to the lithiophilic O and N heteroatoms in PDA, providing multiple deposition sites for Li$^+$ ions, decreasing the nucleation overpotential. The comparative test of CF electrode (without PDA modification) proves the superiority of lithiophilic PDA. As shown in Supplementary Fig. S5a, the CF electrode has a deeper voltage drop and a larger nucleation overpotential at different current densities. The morphology of deposited lithium (Supplementary Fig. S5b) shows local accumulation rather than uniform distribution. These comparisons display the advantage brought by the lithiophilicity of PDA, which overcomes the heterogeneous nucleation barrier of lithium ions on CF and homogenizes lithium deposition.

To cross the heterogeneous nucleation barrier caused by huge thermodynamic mismatch between lithium and copper (poor lithiophilicity), the copper foil possesses a large overpotential of ~100 mV, which leads to a deep drop when starting discharge. Theoretically, the lithium-ion deposition potential is 0 (relative to Li/Li$^+$), but during the discharge process, there are a heterogeneous nucleation barrier, concentration polarization, and ohmic polarization on the electrode surface, all of which result in an overpotential. Therefore, only a negative potential can drive lithium ions to undergo a reduction reaction on the electrode surface to form lithium metal.

The Li/Cu cell was used to monitor the CE and cycling stability to assess the cycling performances of PDA@CF electrode. We adopted two methods to determine the CE. The most common method is depositing a given amount of Li metal (Q_D), and then stripping lithium metal (Q_S) from the copper electrode to a cut-off voltage. The CE can be calculated:

$$CE = \frac{Q_S}{Q_D}$$

As shown in Fig. 4a, except for the first cycle, the CE of the cells using PDA@CF electrode could be stabilized at about 99%
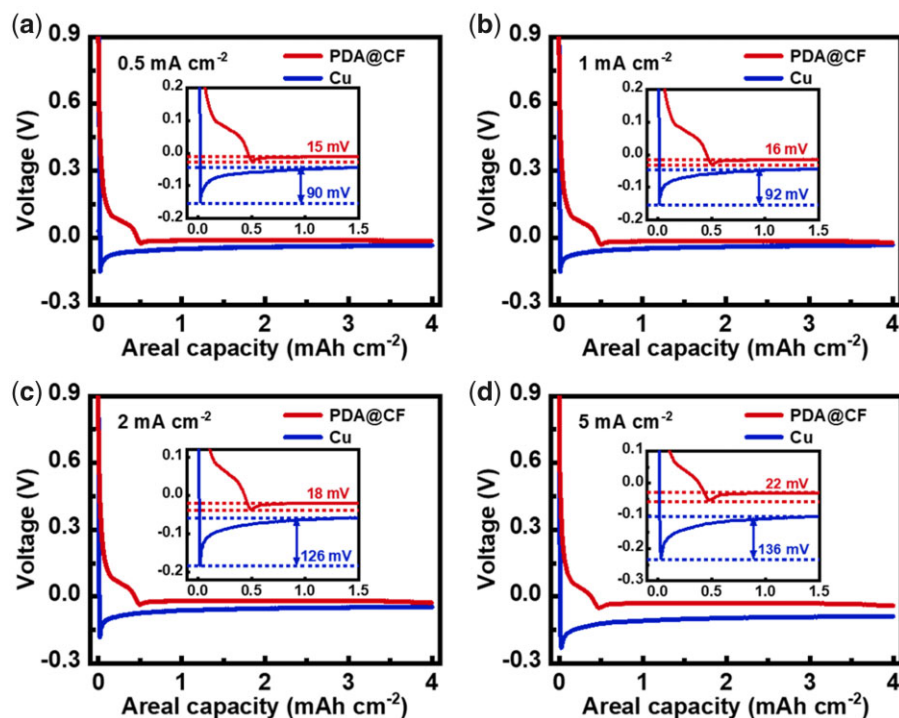
Figure 3: The difference in the discharge curve of Li/PDA@CF and Li/Cu half cells at various current densities of (a) 0.5, (b) 1, (c) 2 and (d) 5 mA cm^{-2}.

under the 0.5 mA cm^{-2} current density for 500 cycles. In contrast, the CE of cells with pristine copper electrode is unstable, sometimes exhibits a low value, and then followed with an abnormally high value (>100%) in later cycles, which is mainly due to the disconnection of dendrites and electrical reconnection of 'dead' lithium. When the current density further rises to 1 and 2 mA cm^{-2}, the PDA@CF cells still present a CE of about 98.2% and 97.8%, respectively. However, the cells using Cu display poor cycling performance with fluctuant CE and shorter lifetimes. The CE of Li/Cu cells shows a continuous decrease after 120 cycles under 1 mA cm^{-2} and 50 cycles under 2 mA cm^{-2} because of the irreversible formation of unreactive 'dead' lithium. When rising to a high current density of 5 mA cm^{-2}, PDA@CF could deliver a high CE of about 97% for over 400 cycles, exhibiting more stability than that of the pristine copper electrodes. More prominently, when further increasing the deposition capacity, the PDA@CF electrode could maintain excellent cycling with a high CE (Supplementary Figs S6 and S7). Especially under the current density of 2 mA cm^{-2} and the capacity of 4 mAh cm^{-2}, stable 200 cycles could be achieved with a high CE of ~95.8%. In comparison, the CE of Cu exhibits rapid decay after 50 cycles under extreme conditions. Figure 4b and c shows the detailed voltage curves of Li depositing/stripping under the 5 mA cm^{-2} current density. The cells using the PDA@CF electrode possess almost identical voltage curves in different cycles, accompanied by low voltage hysteresis of ~60 mV. Such outstanding performance is mainly due to the numerous deposition sites on the PDA guiding the uniform deposition of lithium, reducing the cell polarization and thus preventing the growth of lithium dendrites. In comparison, pristine Cu manifests terrible Li plating/stripping behaviors. As the increase of cycles, the charging voltage profiles of pristine Cu shift leftward gradually, which indicates the existence of 'dead' lithium, leading to massive irreversible capacity loss. Supplementary

Table S1 compares the CE of the PDA@CF electrode with results from a wide variety of previous state-of-art studies.

During the lithium depositing process, Li loss includes the side reaction of Li with electrolyte or Cu substrate surface [37]. To eliminate the possible lithium loss caused by the substrate, we choose another charge/discharge mode to measure CE. An excess given amount of Li metal (Q_T) is deposited onto the copper electrode as a lithium reservoir in the initial cycle, and then a small part of lithium (Q_C) is utilized to plate and strip. After running for n cycles, stripping the remaining Li metal (Q_S) from copper electrode to a cut-off voltage. The average CE for n cycles could be calculated:

$$CE_{avg} = \frac{nQ_C + Q_S}{nQ_C + Q_T}$$

In the practical LMBs, lithium metal is not completely stripped from the substrate, so the CE_{avg} measured by this method can better reflect the practical situation of the electrode. Under the current density of 1, 2 mA cm^{-2}, the initial Q_T of 6 mAh cm^{-2} and cycling Q_C of 0.5 mAh cm^{-2} (Fig. 5a and b), PDA@CF shows excellent cycling stability, illustrated by the lower polarization overpotential, and smooth delithiation process in the last cycle, which exhibits the high CE_{avg} of 99.6% and 99.5%, respectively. By contrast, the cells using pristine Cu foil show larger overpotential and inferior stripping behaviors, such as the fluctuant voltage curves. As the amount of cycling lithium (Q_C) increasing to 1 mAh cm^{-2} (Supplementary Fig. S8), the copper foil displays worse cycling behaviors. Particularly at the 2 mA cm^{-2} current density (Supplementary Fig. S8b), the voltage rises with several abrupt drops in the last cycle, indicating the existence of micro short circuit triggered by lithium dendrite puncture. While the dendrites piercing the separator and contacting the counter electrode, the short circuit for a moment generates heat and melts the tips of dendrites, so the voltage
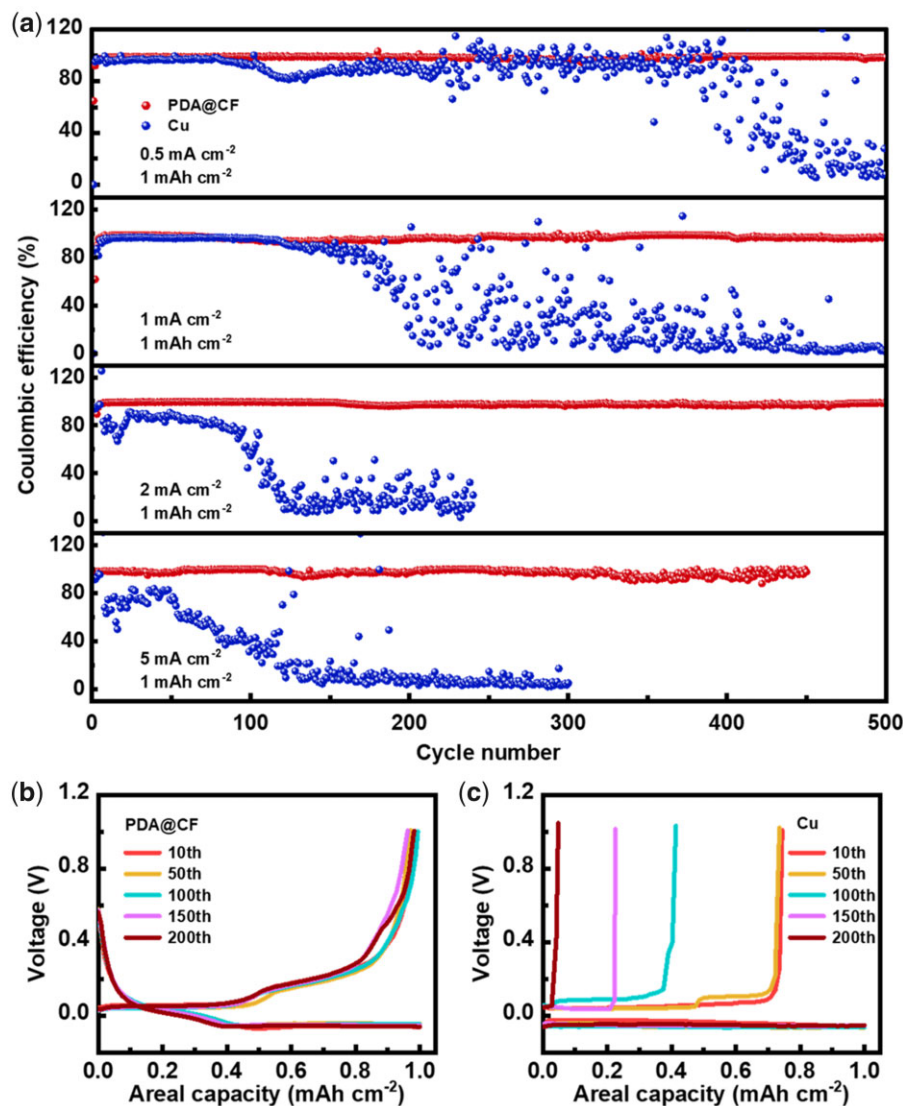
Figure 4: (a) CE of lithium depositing on PDA@CF electrode and pristine Cu foil at different current densities of 0.5, 1, 2 and 5 mA cm^{-2} with a fixed 1 mAh cm^{-2} deposition capacity. (b and c) Voltage curves of the lithium depositing/stripping process on (b) PDA@CF electrode and (c) pristine Cu foil under the 5 mA cm^{-2} current density of and a fixed 1 mAh cm^{-2} deposition capacity.

drops in a short time and then rises normally. The amount of electricity that flows through in a short circuit is counted as part of the charging capacities, so causing the illusion that the CE$_{avg}$ exceeds 100%. However, the PDA@CF electrode still maintains stable cycling and high CE$_{avg}$ nearly to 99% under the test condition of the Q$_C$ of 1 mAh cm^{-2}, deriving from the uniform lithium deposition and storage in 3D CFs skeleton and less Li loss caused by side reactions.

Galvanostatic cycling test was accomplished in symmetrical cell to further evaluate the cycling stability of PDA@CF electrode. The PDA@CF and copper electrode were electrochemically pre-deposited with a fixed amount of Li metal (deposition capacity of 6 mAh cm^{-2}, equal to a specific capacity of 677 mAh g^{-1} base on the total mass), and tested under the 1 mA cm^{-2} current density and 1 mAh cm^{-2} cycling capacity. Figure 6a shows the voltage–time profiles, which could be utilized to analyze the stability of electrodes. Noticeably, the PDA@CF-Li exhibited superior cycling performance in 1000h with a low overpotential (~12 mV). However, the Cu-Li cells

display an unstable voltage profile with a high overpotential over 30 mV and violent fluctuation at first 650 cycles. After 700 cycles, the overpotential value presents a rapid decrease, indicating that a short circuit occurred inside the cell. To show the detailed evolution of voltage curves, 100–108 and 346–354 cycles of symmetric cell are enlarged in Fig. 6b and c. The PDA@CF-Li symmetric cells maintained even voltage plateaus at charge/discharge processes throughout the 1000 h. In comparison, the Cu-Li cells displayed unstable voltage jitter especially after long-term cycling, resulting from the uncontrolled lithium dendrites and continuous consumption of electrolytes. In addition, under the higher current density of 2, 5 mA cm^{-2} (Supplementary Figs S9 and S10), the PDA@CF-Li still maintained excellent stability and lower overpotential, while Cu-Li electrode exhibits inferior cycling performance and shorter cycling life. The voltage variation of the cell could be accurately revealed from the voltage hysteresis, which could be defined as the voltage gap between the lithium depositing and stripping [38]. As shown in Fig. 6d, the voltage hysteresis of Cu-Li cell
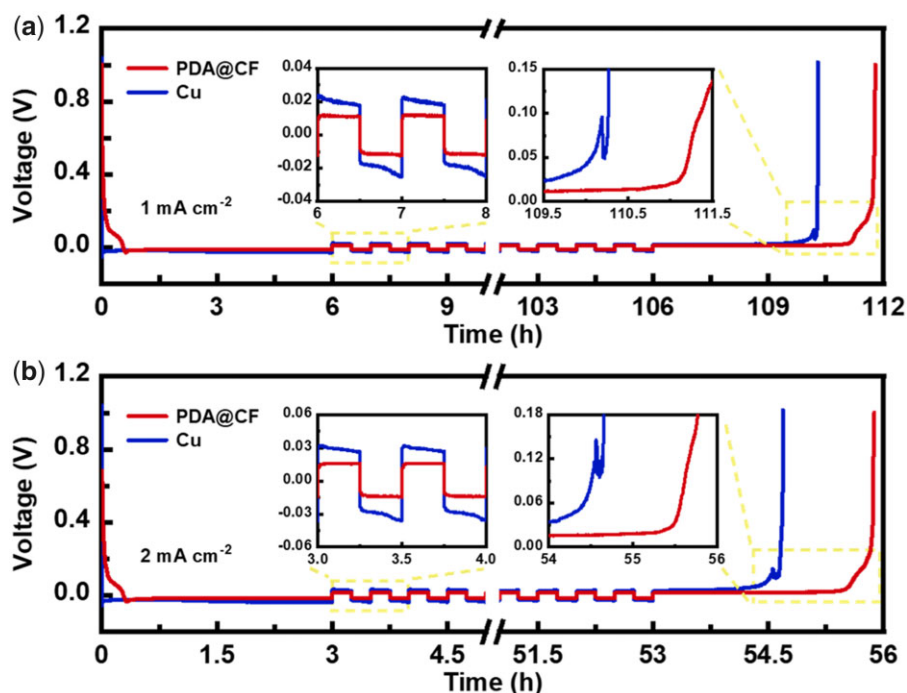
Figure 5: The voltage versus time plot in CE evaluation test on PDA@CF electrode and pristine copper electrode under the current densities of (**a**) 1 and (**b**) 2 mA cm^{-2} with constant Q_C of 0.5 mAh cm^{-2}.
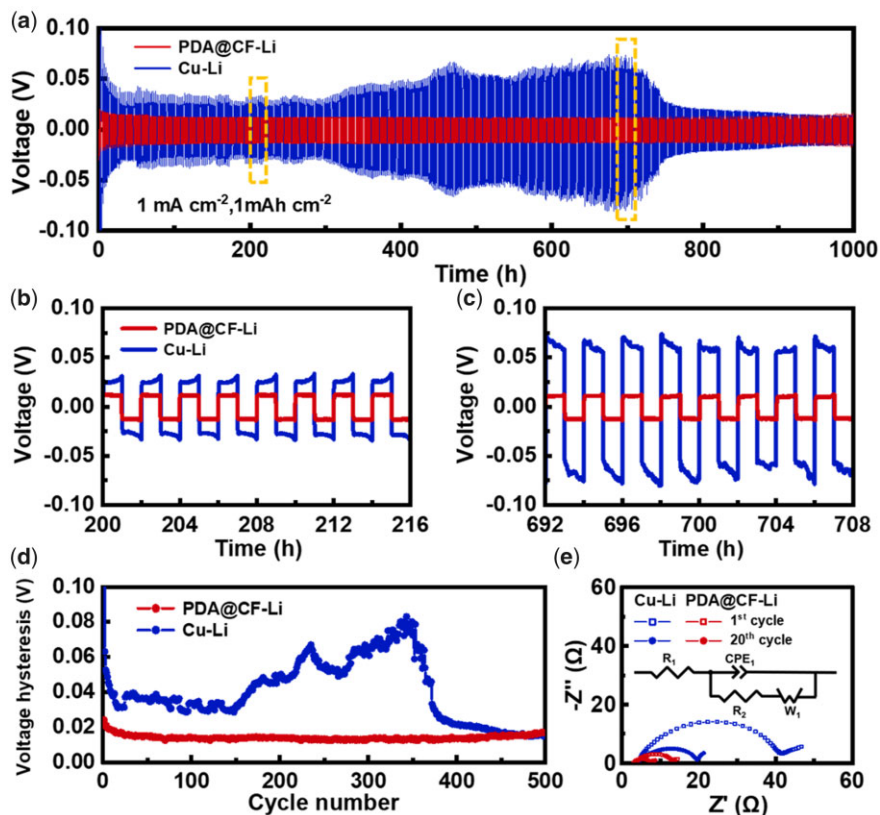

Figure 6: (**a**) Galvanostatic cycling curves of Cu-Li and PDA@CF-Li symmetric cells at 1 mA cm^{-2} current density and 1 mAh cm^{-2} cycling capacity. And the corresponding detailed voltage curves from (**b**) 200 h to 216 h and (**c**) 692 h to 708 h. (**d**) Voltage hysteresis of the PDA@CF-Li and Cu-Li symmetric cells at 1 mA cm^{-2} current density and 1 mAh cm^{-2} cycling capacity. (**e**) The impedance spectra of the PDA@CF-Li and Cu-Li symmetric cells at 1st and 20th cycle under 1 mA cm^{-2}.
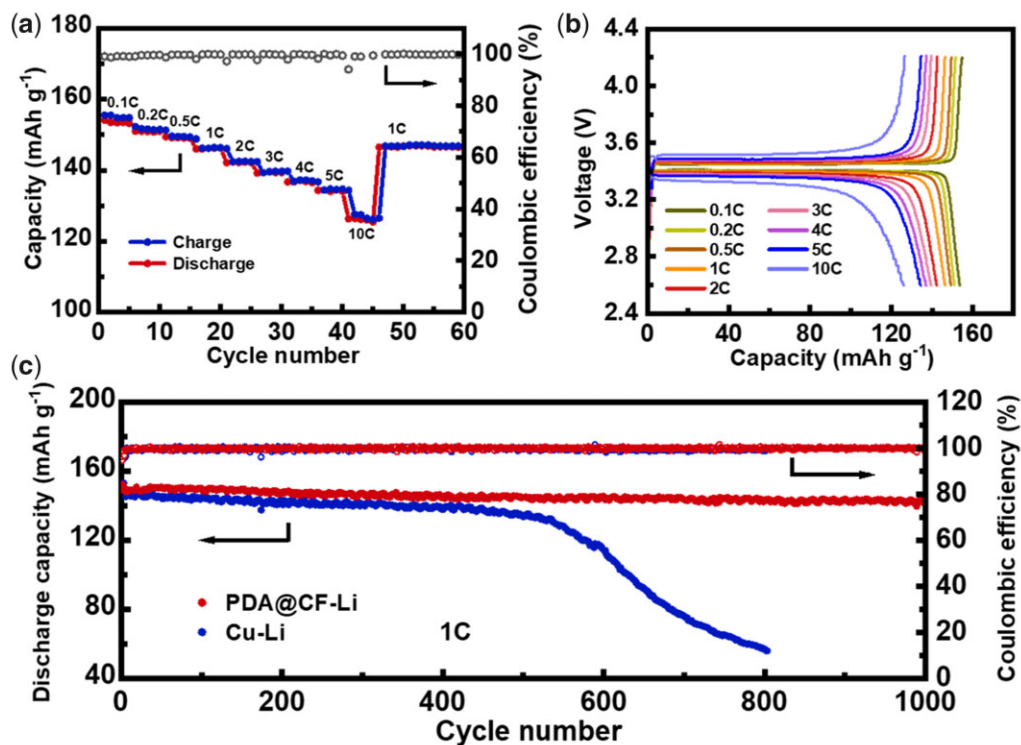
Figure 7: (a) Rate performance of PDA@CF-Li/LFP cell. (b) Charge/discharge voltage curves of PDA@CF-Li/LFP cell at various current densities. (c) Long-term cycling performance of Cu-Li/LFP and PDA@CF-Li/LFP cells under the current density of 1 C.

increases continuously after 150 cycles with temporary irregular fluctuation. In contrast, the PDA@CF-Li symmetric cells always remain stable, and the voltage hysteresis is only about 16 mV, indicating the processes of uniform Li plating/stripping. Furthermore, EIS measurements of the symmetric cells were completed to evaluate the interfacial resistance and stability (Fig. 6e). The inset of Fig. 6e shows the equivalent circuit utilized to fit the impedance spectra, including bulk resistance (R_1), interface resistance (R_2), constant phase element (CPE_1) and Warburg resistance (W_1). In the impedance spectra, the semicircle at the high-frequency range shows the charge transfer resistance and interfacial resistance between the electrolyte and electrode [39]. The cell using Cu-Li displayed a high interfacial resistance (∼40 Ω) after one cycle, which is almost 4 times that of cell using PDA@CF-Li. After twenty cycles, the interfacial resistance of Cu-Li (15.3 Ω) is still higher than that of the PL-Li (4.2 Ω), demonstrating the faster Li plating/stripping reaction kinetics and lower hysteresis of PDA@CF-Li.

The PDA@CF-Li and Cu-Li anodes (with 6 mAh cm^{-2} predeposited Li) were paired with LiFePO$_4$ to study full cell cycling performance. Figure 7a, b show the rate performance and the detailed charge/discharge voltage curves of PDA@CF-Li/LFP cells at various current densities. Compared with the Cu-Li/LFP cell (Supplementary Fig. S11), the PDA@CF-Li/LFP cell exhibit minor polarization potential and more stable voltage plateaus, especially at high rates. PDA@CF-Li/LFP cells render discharge capacity of 135 and 127 mAh cm^{-2} at 5 C and 10 C, respectively. In comparison, Cu-Li/LFP cells offer the lower capacity of 126 and 111 mAh cm^{-2} at 5 C and 10 C, respectively. Besides, the effective dendrite inhibition by PDA@CF ensures ultra-long cycling performance. As shown in Fig. 7c, PDA@CF-Li/LFP cells display outstanding stability for 1000 cycles with little changes in discharge capacity from 148.6 mAh g^{-1} (1st cycle) to 142.4 mAh g^{-1}

(1000th cycle), which corresponds to high capacity retention (95.8%). However, the Cu-Li/LFP cells show poor cycling performance, the discharge capacity decays rapidly from 137.9 mAh g^{-1} to about 50 mAh g^{-1} after 400 cycles, and the capacity retention is below 37%. Moreover, another long-term cycling under a higher current density of 2 C was completed. The discharge capacities for the two cells are almost identical in the first few cycles (Supplementary Fig. S12). However, the capacity of the Cu-Li/LFP cells decreases gradually after 250 cycles, while cells with PDA@CF-Li anode deliver stable cycling performance over 1000 cycles without obvious capacity loss. In ordinary graphite/LFP batteries which the graphite possesses a specific capacity of 372 mAh g^{-1}, the SEI film formation consumes a number of lithium ions in the first cycle, leading to a decrease in the CE of the battery. When the PDA@CF-Li electrode (pre-deposition capacity of 6 mAh cm^{-2}, a specific capacity of 677 mAh g^{-1}) is used, the deposited lithium can supplement the consumed lithium capacity, thereby maintaining a high CE.

The pure lithium metal anode has a larger capacity than the PDA@CF-Li at the initial stage of electrochemical cycling, but as the number of cell cycles increases, the 'hostless' lithium anode inevitably produces lithium dendrites and 'dead' lithium, which greatly reduces the usable capacity. To balance capacity and life, it is probably more effective to use a modified current collector (PDA@CF) to obtain a longer cycle life when the volumetric capacity of the negative electrode is only slightly reduced.

CONCLUSIONS

In summary, a 3D porous lithiophilic PDA@CF electrode was created to achieve excellent cycling performance and stable lithium plating/stripping in LMBs. The conductive 3D CFs not only reduce the local current density but also serve as the host to

accommodate deposited Li metal, which can alleviate the large volume change of lithium metal. Moreover, the significant amount of lithiophilic O and N-based polar groups in PDA has strong interaction with Li^+, which can homogenize Li^+ distribution and decreases the nucleation overpotential. Under the synergy of PDA and CF, the PDA@CF could effectively improve the electrochemical behaviors of Li^+ ions, show an extremely high CE of 98.2% at 1 mA cm^{-2} for 500 cycles. In symmetric cells, the PDA@CF-Li anode showed ultra-stable cycling life accompanied by a low overpotential of 12 mV, and 1000h duration can be achieved under 1 mA cm^{-2}. When paired with LFP cathode, excellent long-term stability for 1000 cycles with high CE of about 100% can be realized. The combination of both uniform Li nucleation and storage in the design of PDA@CF in this work is expected to be general for the designs of stable lithium metal anode.

SUPPLEMENTARY DATA

Supplementary data is available at *Oxford Open Materials Science* online.

FUNDING

AUTHOR'S CONTRIBUTIONS

L.X. made a major contribution to the article, including idea, materials synthesis, battery tests and initial draft. Z.Y. provided important experimental insights. J.Z. as the corresponding author, critically reviewed the article and made revisions.

CONFLICT OF INTEREST STATEMENT

The authors declare no conflict of interest.

REFERENCE

1. Scrosati B. History of lithium batteries. *J Solid State Electrochem* 2011;**15**:1623–30.
2. Pan Q, Guo K, Wang L. Novel modified graphite as anode material for lithium-ion batteries. *J Electrochem Soc* 2002;**149**:A1218–A1223.
3. Tarascon MJ. Key challenges in future Li-battery research. *Philos Trans R Soc A Math Phys Eng Sci* 2010;**368**:3227–41.
4. Zhang H, Li X, Zhang H. *Li–S and Li–O2 Batteries with High Specific Energy*. Singapore: SpringerBriefs in Molecular Science, 2017.
5. Bruce PG, Freunberger SA, Hardwick LJ et al. Li-O2 and Li-S batteries with high energy storage. *Nat Mater* 2011;**11**:19–29.
6. Whittingham MS. Electrical energy storage and intercalation chemistry. *J Solid State Chem* 1976;**192**:1126–7.
7. Xu W, Wang J, Ding F et al. Lithium metal anodes for rechargeable batteries. *Energy Environ Sci* 2014;**7**:513–37.
8. Yamaki JI, Shin-ichi T, Katsuya H et al. A consideration of the morphology of electrochemically deposited lithium in an organic electrolyte. *J Power Sources* 1998;**74**:219–27.
9. Steiger J, Kramer DM, Nig R. Microscopic observations of the formation, growth and shrinkage of lithium moss during electrodeposition and dissolution. *Electrochim Acta* 2014;**136**:529–36.
10. Smith AJ, Burns JC, Zhao X et al. A high precision coulometry study of the SEI growth in Li/graphite cells. *J Electrochem Soc* 2011;**158**:A447–52.
11. Bieker G, Winter M, Bieker P. Electrochemical in situ investigations of SEI and dendrite formation on the lithium metal anode. *Phys Chem Chem Phys* 2015;**17**:8670–8679.
12. Lin D, Liu Y, Cui Y. Reviving the lithium metal anode for high-energy batteries. *Nat Nanotechnol* 2017;**12**:194–206.
13. Bhatt M, O'Dwyer C. Solid electrolyte interphases at Li-ion battery graphitic anodes in propylene carbonate (PC)-based electrolytes containing FEC, LiBOB, and LiDFOB as additives. *Chem Phys Lett* 2015;**618**:208–13.
14. Lindgren F, Xu C, Niedzicki L et al. SEI formation and interfacial stability of a Si electrode in a LiTDI-salt based electrolyte with FEC and VC additives. *ACS Appl Mater Interfaces* 2016;**8**:15758.
15. Han T, Zheng D, Song P et al. Theoretical study on fluoroethylene carbonate as an additive for the electrolyte of lithium ion batteries. *Chem Phys Lett* 2021;**771**:138538.
16. Ding F, Xu W, Graff GL et al. Dendrite-free lithium deposition via self-healing electrostatic shield mechanism. *J Am Chem Soc* 2013;**135**:4450–6.
17. Zhang Y, Qian J, Xu W et al. Dendrite-free lithium deposition with self-aligned nanorod structure. *Nano Lett* 2014;**14**:6889–96.
18. Osaka T, Momma T, Matsumoto Y et al. Effect of carbon dioxide on lithium anode cycleability with various substrates. *J Power Sources* 1997;**68**:497–500.
19. Lei T, Xue L, Li Y et al. Enhanced electrochemical performances via introducing LiF electrolyte additive for lithium ion batteries. *Ceram Int* 2019;**45**:18106–10.
20. Han X, Sun J. Design of a LiF-rich solid electrolyte interface layer through salt-additive chemistry for boosting fast-charging phosphorus-based lithium ion battery performance. *Chem Commun* 2020;**56**:6047–6049.
21. Eftekhari A, Liu Y, Chen P. Different roles of ionic liquids in lithium batteries. *J Power Sources* 2016;**334**:221–39.
22. Wang Z, Cai Y, Tao D et al. Triethylbutylammonium bis(trifluoromethanesulphonyl)imide ionic liquid as an effective electrolyte additive for Li-ion batteries. *Ionics* 2013;**19**:887–94.
23. Ho V-C, Ngo DT, Le HTT et al. Effect of an organic additive in the electrolyte on suppressing the growth of Li dendrites in Li metal-based batteries. *Electrochim Acta* 2018;**279**:213–23.
24. Cai Z, Liu Y, Zhao J et al. Tris(trimethylsilyl) borate as electrolyte additive to improve performance of lithium-ion batteries. *J Power Sources* 2012;**202**:341–6.
25. Liu Y, Lin D, Yuen PY et al. An artificial solid electrolyte interphase with high Li-ion conductivity, mechanical strength, and flexibility for stable lithium metal anodes. *Adv Mater* 2017;**29**: 1605531.
26. Xu R, Zhang X-Q, Cheng X-B et al. Artificial soft-rigid protective layer for dendrite-free lithium metal anode. *Adv Funct Mater* 2018;**28**:1705838.
27. Liu F, Xiao Q, Wu HB et al. Fabrication of hybrid silicate coatings by a simple vapor deposition method for lithium metal anodes. *Adv Energy Mater* 2018;**8**:1701744.
28. Wang C, Fu K, Kammampata SP et al. Garnet-type solid-state electrolytes: materials, interfaces, and batteries. *Chem Rev* 2020;**120**: 4257–4300.
29. Takada K. Progress and prospective of solid-state lithium batteries. *Acta Mater* 2013;**61**:759–770.

30. Chen R, Qu W, Xing G et al. The pursuit of solid-state electrolytes for lithium batteries: from comprehensive insight to emerging horizons. *Mater Horizons* 2016;**3**: 487–516.

31. Manthiram A, Yu X, Wang S. Lithium battery chemistries enabled by solid-state electrolytes. *Nat Rev Mater* 2017; **2**(10app.):16103.

32. Hou G, Ren X, Ma X et al. Dendrite-free Li metal anode enabled by a 3D free-standing lithiophilic nitrogen-enriched carbon sponge. *J Power Sources* 2018;**386**:77–84.

33. Jin C, Sheng O, Luo J et al. 3D lithium metal embedded within lithiophilic porous matrix for stable lithium metal batteries. *Nano Energy* 2017;**37**:177–86.

34. Lee H, Song J, Kim YJ et al. Structural modulation of lithium metal-electrolyte interface with three-dimensional metallic interlayer for high-performance lithium metal batteries. *Sci Rep* 2016;**6**:30830.

35. Shen F, Zhang F, Zheng Y et al. Direct growth of 3D host on Cu foil for stable lithium metal anode. *Energy Storage Mater* 2018; **13**:323–8.

36. Zhai P, Wei Y, Xiao J et al. In situ generation of artificial solid-electrolyte interphases on 3D conducting scaffolds for high-performance lithium-metal anodes. *Adv Energy Mater* 2020; **10**:1903339.

37. Adams BD, Zheng J, Ren X et al. Accurate determination of coulombic efficiency for lithium metal anodes and lithium metal batteries. *Adv Energy Mater* 2018;**8**:1702097.

38. Zheng G, Lee SW, Zheng L et al. Interconnected hollow carbon nanospheres for stable lithium metal anodes. *Nat Nanotechnol* 2014;**9**:618–23.

39. Zhang W, Zhuang HL, Fan L et al. A "cation-anion regulation" synergistic anode host for dendrite-free lithium metal batteries. *Sci Adv* 2018;**4**:eaar4410.